

Spatial-temporal behaviors of low-Stokes-number particles forming coherent structures in high-aspect-ratio liquid bridges by thermocapillary effect

Shin Noguchi

*Division of Mechanical and Aerospace Engineering, School of Science and Technology,
Tokyo University of Science, 2641 Yamazaki, Noda, Chiba 278-8510, Japan*Ichiro Ueno ^{*}*Department of Mechanical and Aerospace Engineering, Faculty of Science and Technology,
Tokyo University of Science, 2641 Yamazaki, Noda, Chiba 278-8510, Japan*

(Received 2 July 2022; accepted 29 August 2023; published 9 November 2023)

We investigate experimentally coherent structures of low-Stokes-number particles in the thermocapillary liquid bridge as a closed system. Such coherent structures in thermocapillary liquid bridges have been known as particle accumulation structures (PASs) realized in traveling-wave-type convection. We discover the PAS in the flow of $m = 1$ in an azimuthal wave number in the liquid bridge of $O(10^{-3}\text{m})$, whose spatial structure is different from those hitherto indicated in previous research, with the particles heavier than the test liquid. The coherent structures by the particles suspended in the liquid bridge are illustrated in the laboratory frame and in the rotating frame of reference. Individual particles of Stokes number $St = O(10^{-5})$ are tracked to indicate their spatial-temporal behaviors forming the coherent structures. We unveil that two major coherent structures are simultaneously emanated inside the liquid bridge of $\Gamma = 1.6$ in aspect ratio. Their Poincaré sections are illustrated, which well reproduce qualitatively the predictions of Barmark *et al.* [*Phys. Rev. Fluids* **6**, 084301 (2021)].

DOI: [10.1103/PhysRevFluids.8.114002](https://doi.org/10.1103/PhysRevFluids.8.114002)

I. INTRODUCTION

Control of particle distributions in closed multiphase-flow systems has attracted attention in both industrial and natural fields. In industrial fields, such problems commonly arise in a variety of processes such as chemical, material, pharmaceutical, paper, and food engineering. Separation and sorting tiny particles are essential techniques for crystal growth processes [1–5] and microdevices [6–9]. Environmental control of chemical contaminants in clean rooms [10] is another example. In nature, we have faced serious problems of pollution by microplastics [11–16]. One finds such problems in air pollution by soil and sea salt particles [17] and flow patterns in rivers [18] as well.

In closed systems, it has been known that suspended tiny particles distribute unevenly to form coherent structures in laminar flows after the pioneering work by Schwabe *et al.* [19]: The tiny particles suspended in the liquid as tracers gather to form a structure, which was named the particle accumulation structure (PAS). Schwabe *et al.* [19] found that such unique patterns by the particles arise in traveling-wave-type convection fields induced by so-called hydrothermal-wave (HTW) instability [20] in half-zone liquid bridges of high-Prandtl-number liquid. Takakusagi and Ueno [21] indicated the PAS emerges in hanging droplets, which is also caused by thermocapillary effect.

*ich@rs.tus.ac.jp

Romanò *et al.* [22] and Wu *et al.* [23] indicated that the particle accumulations are realized not only in thermocapillary liquid bridges but also in the lid-driven cavity of isothermal systems.

A number of research on the coherent structures by the particles has been conducted by employing so-called half-zone liquid bridges after Schwabe *et al.* [19]. A certain amount of liquid bridges the end surfaces of coaxial circular rods: One rod is heated and the other is cooled to induce a designated temperature difference between the end surfaces of the liquid bridge. This temperature difference results in driving the fluid over the free surface, which is due to the temperature dependence of the surface tension. This geometry was proposed by mimicking a half portion of full-zone liquid bridges for, e.g., semiconductor crystal growth processes [24–28], and has been widely employed in fundamental experimental research on the thermocapillary-driven convection under the normal gravity condition e.g., [29–41] and the microgravity conditions e.g., Refs. [42–54]. The advantage of this geometry comes from the simpler thermal boundary condition than that in the full-zone ones: The intensity of the thermocapillary effect is defined by considering the nondimensional Marangoni number $Ma = |\gamma_T| \Delta T L / (\rho \nu \kappa)$, where $\gamma_T = \partial \gamma / \partial T$ is the temperature coefficient of surface tension γ , ΔT is the temperature difference between the both ends of the liquid bridge, L is the characteristic length, ρ is the density of the test liquid, ν is the kinematic viscosity, and κ is the thermal diffusivity. The Marangoni number is also described as the product of the thermocapillary Reynolds number $Re = |\gamma_T| \Delta T L / (\rho \nu^2)$ and the Prandtl number $Pr = \nu / \kappa$. After the findings by Schwabe *et al.* [19], Tanaka *et al.* [55] conducted a series of experiments to investigate the PAS by varying Ma and the aspect ratio of the liquid bridge, $\Gamma = H/R$, where H is the height of the liquid bridge or the distance between the coaxial rods of R in radius. They illustrated essential features through their experiments: (i) A coherent structure is formed by the particles suspended in the liquid bridge in a limited range of Ma and seems rotating in azimuthal direction without changing its shape as if it were a rigid structure. (ii) The PAS emerges under Ma higher than the threshold for the primary instability $Ma_c^{(1)}$. (iii) The rotating direction of the PAS is the same as the thermal-flow field by the HTW instability, and the particles forming the PAS travel azimuthally opposite to that of the PAS. (iv) The PAS exhibits a structure with the same azimuthal wave number as the thermal flow field induced by the HTW instability, which depends on Γ [31,38,56]. (v) The PAS has the azimuthal periodicity as the flow and is winding m times about the main vortex before closing. They indicated further that (vi) the particles gather not only to form the PAS but also to form a toroidal structure called a core; (vii) two different types of PASs, SL1- and SL2-PASs, emerge by changing Ma under a fixed Γ ; (viii) SL2-PAS emerges under higher Ma than SL1-PAS, and (ix) additional loop structure appears at each tip near the free surface for SL2-PAS. Tanaka *et al.* [55] explored the existing range of the PAS of $2 \leq m \leq 5$ by varying Γ , and Schwabe *et al.* [57] found that the optimum density for PAS formation is density matching and there exists an optimum particle size. Further exploring for the PAS in the HTW of $m = 1$, Schwabe *et al.* [57] found that the existing range for $m = 1$ is significantly narrow in Ma and Γ comparing to those of $m \geq 2$.

In addition, the formation of the tall or high- Γ liquid bridge to realize the PAS in the HTW of $m = 1$ is much more difficult in the first place due to the static pressure under the normal gravity condition. These are the critical reasons why the investigation on the PAS in the HTW of $m = 1$ via terrestrial experiments had not been actively conducted [58–60] and why microgravity experiments have been deserved. The PASs in the HTW of $2 \leq m \leq 5$ have attracted the attention of lead investigations via experimental [55,57,59,61–69] and numerical approaches [70–82].

Mukin and Kuhlmann [83] and Hofmann and Kuhlmann [73] indicated that there exist Kolmogorov-Arnold-Moser (KAM) tori in the traveling-wave-type modeled convection, whose three-dimensional structures in the rotating frame of reference resemble those of the PASs. In the reference frame, the KAMs rigidly form in the flow field, as observed for the PASs [66,67] up to the secondary instability [84]. In particular, the introduction of the rotating frame of reference by Hofmann and Kuhlmann [73] has had a significant impact, enabling quantitative evaluation of particle trajectories and facilitating comparison of stream profiles in experiments. Indeed, it has been revealed by experiments [65,67,68] that several types of PASs coexist simultaneously as the

predicted KAM tori. Oba *et al.* [68] indicated the motion of the particles tracked in two and three dimensions. They successfully reconstructed the three-dimensional motion of the particles forming three different coherent structures: the PAS in the HTW of $m = 3$, the toroidal core, and the structure wrapping the toroidal core.

As for the PAS in the HTW of $m = 1$, on the contrary, few research works have been conducted to accumulate knowledge on the shape of the PASs themselves and the behaviors of the particles forming the coherent structures. Sasaki *et al.* [85] indicated the PASs in the HTW of $m = 1$ under the normal gravity condition by employing the liquid bridge of $\Gamma = 2.1$ whose radius is less than 1mm. They evinced the PAS in the HTW of $m = 1$ in a range of Ma by suspending the particle heavier than the test liquid: The particles form the closed path with a spiral structure in the interior region of the liquid bridge. Sakata *et al.* [59] then realized the similar PAS in the liquid bridges of $\Gamma = 2.0$ under the normal gravity condition and in those of $\Gamma = 1.0$ under microgravity conditions. It must be noted that Sakata *et al.* [59] and Terasaki *et al.* [60] realized the PAS in the HTW of $m = 1$ in the terrestrial experiments by employing a rather slender liquid bridge or whose volume ratio V/V_0 is less than unity, where V is the volume of the liquid bridge itself and V_0 is the volume of the cylinder between the end surfaces, or $V_0 = \pi R^2 H$; the thermal flow field in the liquid bridge of $\Gamma = 2.0$ and of $V/V_0 \sim 1.0$ exhibits the traveling-wave-type oscillation but does not accompany the particle accumulations [86]. Since the late 2010s, the PASs in the HTW of $m = 1$ have been actively investigated via numerical approaches: A group at the University of Strathclyde (Glasgow, Scotland) finely reproduced the PAS with a spiral in the HTW of $m = 1$ in the liquid bridges of $\Gamma = 1.8$ for $Pr = 8$ [87] and $Pr = 68$ [88]. Their coherent structure reproducing the one observed by Sasaki *et al.* [85], however, was realized with particles lighter than the test liquid, or $\varrho = \rho_p/\rho_l < 1$, where ρ_p and ρ_l are the densities of the particles and the test liquid, respectively. Note that the particles of $\varrho > 1$ form the coherent structure in the HTW of $m = 1$ [59,60,85] as well as those of $m \geq 2$ [55,57,62,63,67,68,89] by experiments. A group of TU Wien (Austria) also demonstrated the PAS of $m = 1$ in the liquid bridge of $\Gamma = 1$ and $Pr = 68$ [90–92]. The group reproduced the PASs with neutral-buoyancy particles [90,91] and with particles of various densities [92]. Barmak *et al.* [92] demonstrated the structure of the KAM tori for several Re under which the flow is temporally and spatially periodic. They discussed the dependence of the PAS on the particle size, the density ratio of the particle to the test liquid (ϱ), and Re . They also investigated the effect of the interaction parameter between the free surface and the particle (Δ); this parameter indicates the position where a particle approaching the free surface experiences an inelastic collision, and where its velocity component normal to the boundary is annihilated from the flow boundary. Under a condition of small Δ and higher Re , the PAS with a spiral structure, as observed in the terrestrial [59,60,85] and microgravity [59] experiments, was predicted. Knowledge has been thus far accumulated on the PASs in the HTW of $m = 1$ via the numerical simulations by different research groups, but little evidence via the experimental approaches has been indicated. It must be remarked, in the case of the PASs of $2 \leq m \leq 4$, that the numerical works successfully reproduced the shape of the PASs independently: The predicted PAS consisted of m -fold blades [70–82] as noted, although there exist minor discrepancies in the characteristics of the blades such as the azimuthal width and the minimum and maximum radial positions. In the case of the PAS in the HTW of $m = 1$, on the contrary, the PASs of completely different spatial structures have been predicted by different groups. Further, the PAS with a spiral in the HTW of $m = 1$ is a single example that has been experimentally indicated under normal [59,60,85] and microgravity [59] conditions.

In the present paper, we devote ourselves to revealing the existence of different types of PASs in the HTW of $m = 1$. Through the three-dimensional tracking of the particles forming the PASs, the spatial structures of the PASs and the corresponding Poincaré section of the particles forming the coherent structures are illustrated. We then indicate two different types of PASs coexisting in the liquid bridge. Their discrepancy is discussed with the temporal correlation between the HTW and the particle motions in the rotating frame of reference. Comparisons are made in the Poincaré sections between the PASs by the experiments and the ordered flow structures of the KAM tori predicted.

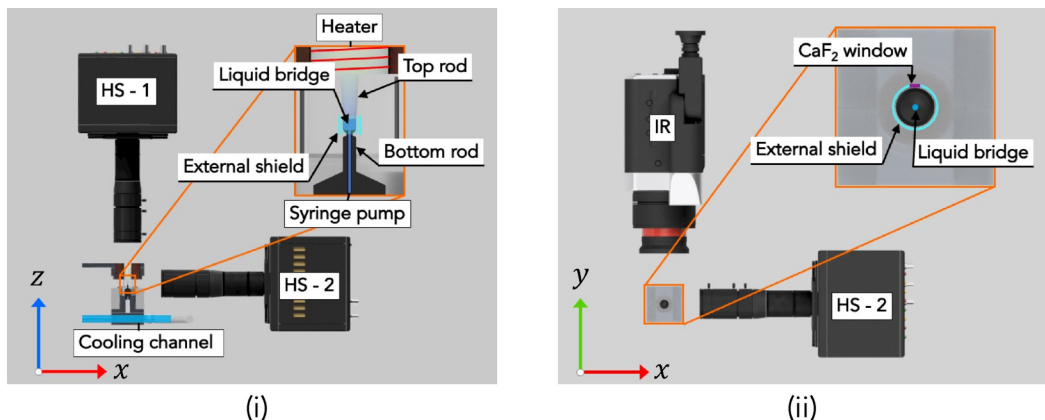


FIG. 1. Experimental apparatus: (i) Side view and (ii) top view. Enlarged schematics of the liquid-bridge holding part is drawn in each frame.

II. METHODS

Figure 1 illustrates a schematic of the experimental setup. The apparatus in the present study is the same as introduced by Sakata *et al.* [59] for the terrestrial experiments and by Terasaki *et al.* [60]. The apparatus consists of two main parts: the one that holds the liquid bridge and realizes the prescribed environment and the other that measures and accumulates the data of particle images and temperature. The liquid-bridge holding part consists of top and bottom rods installed coaxially. The radius of the end surfaces of the both rods is $R = 0.75$ mm. The top rod is made of sapphire, which is colorless and transparent. This property allows us to monitor the motion of particles through the rod. The top rod is heated by a nichrome wire heater wrapped around the rod, whose temperature T_H is measured by a K-type thermocouple embedded in the rod. The heater and the thermocouple are connected to the temperature controller (Model 335 Cryogenic Temperature Controller, Lake Shore Cryotronics Inc., USA) to realize the designated T_H by the proportional-integral-derivative control. The thermocouples in the present system are calibrated using a platinum temperature resistance: Their accuracy is of ± 0.5 K in the range of 50°C to 70°C . The bottom rod is made of aluminum, whose surface is anodized in black to improve corrosion and wear resistance. In addition, the upper edge of the lower rod is tapered at 45° and is coated with fluorine to prevent undesigned liquid dripping from the rod. The temperature of the bottom rod is controlled at $T_C = 20^\circ\text{C}$ by using a cooling channel through its base block. The error in ΔT is thus of $\pm 1\text{K}$, which results in the error in Ma of $\pm 5\%$. Note that the characteristic length L is defined by the height of the liquid bridge H throughout the present paper. A hole with a radius of 0.15 mm is drilled along the center of the bottom rod to form a channel connected by a tube to a syringe filled with the test liquid. The liquid supply from the syringe is controlled by a syringe pump. The velocity of the injected liquid is less than $3.0 \times 10^{-6}\text{m/s} \ll U_\gamma = |\gamma_T| \Delta T / (\rho \nu)$; the rate of the liquid supply is sufficiently small to avoid undesigned disturbances to the flow field and particle behaviors [59,60,68]. The test liquid used in this series of experiments is 2-cSt silicone oil (KF96L-2cs, Shin-Etsu Chemical Co., Japan) whose Pr is of 28.6 at 25°C . The physical properties of the test liquid are listed in Table I. We adopt the mean value of ν for T_H and T_C as the characteristic viscosity to evaluate Ma ; $\nu = \{\nu(T_H) + \nu(T_C)\}/2$. The temperature dependence of the kinematic viscosity is considered by applying an empirical correlation [93] as $\nu(T)/\nu_0 = \exp\{5.892(25 - T)/(273.15 + T)\}$, where ν_0 is the kinematic viscosity of the test liquid at 25°C , and T is the temperature in Celsius. We examine the effects of gravity on the liquid-bridge shape and the thermal-flow fields by considering the static and dynamic Bond numbers defined as $\text{Bo} = \rho g H^2 / \gamma_0$ and $\text{Bd} = \rho g \beta H^2 / |\gamma_T|$, respectively, where g is the gravitational acceleration and β is the thermal expansion coefficient. The

TABLE I. Physical properties of test liquid (2-cSt silicone oil) at 25 °C.

ν_0 [m ² /s]	ρ [kg/m ³]	κ [m ² /s]	β [1/K]	γ_0 [N/m]	γ_T [N/(m K)]	Pr
2.0×10^{-6}	8.73×10^2	7.00×10^{-8}	1.24×10^{-3}	18.3×10^{-3}	-7×10^{-5}	28.6

static and dynamic Bond numbers become $Bo = 0.67$ and $Bd = 0.22$, respectively. To evaluate nondimensional numbers, the values at 25 °C are adopted for all physical properties except ν . The advantage of using silicone oil is that it is highly transparent, which realizes observation of the behavior of particles inside the liquid bridge with visible light. In addition, it is easy to define Ma because the surface tension varies linearly with temperature. The viscosity of 2 cSt is chosen for the following reasons. To reach the high Ma condition under which the PAS emerges steadily in this system, it is supposed to increase the temperature difference between the rods (ΔT) or the characteristic length [= height of the liquid bridge (H)], otherwise to reduce the kinematic viscosity (ν). In ground experiments, there is a severe limitation in realizing the high- Γ liquid bridge, as remarked, to minimize the deviation of the liquid bridge shape from the cylindrical one. Evaporation is also unavoidable when dealing with low-viscosity liquids exposed to a large ΔT . Conversely, with high-viscosity liquids, the temperature of the heated disk must be raised to achieve high Ma , which might result in dangerous situation with a high temperature near the ignition point of the test liquid. From the above reasons, 2-cSt silicone oil has been chosen as the optimal test liquid for this series of experiments.

Gold-nickel-alloy coated acrylic particles (MX-1000NA, Soken Chemical and Engineering Co. Ltd., Japan) are employed as the test particles. The diameter and density of these particles on average are of 10.5 μm and $2.06 \times 10^3 \text{ kg/m}^3$, respectively. The Stokes number of the particles is evaluated by the definition as $St = \rho d_p^2 / (18H^2)$ [73], where d_p is the particle diameter and ρ is the density defined as $\rho_p / \rho = 2.36$, to be of $St = 1.00 \times 10^{-5}$.

The liquid bridge is surrounded concentrically by an acrylic shield of 7.45 mm in inner diameter and of 3 mm in thickness to fix the thermal boundary conditions around the liquid bridge as much as possible. A CaF_2 window (of 2 mm in width, 6 mm in height, and 3 mm in thickness) is installed in a part of the shield, which allows us to measure the surface temperature by an infrared (IR) camera (Thermography R300, NEC Avio Infrared Technologies Co., Ltd., Japan) with a close-up lens (TVC-2100UB, NEC Avio Infrared Technologies Co, Ltd., Japan). We obtain the IR images of 320×240 pixels under a temperature resolution of 0.05 K at 30 °C at 60 frames per second (fps). This IR camera detects the IR light in a range of 8 μm to 14 μm in wavelength. It should be noted that it is rather difficult to measure the exact temperature of the free surface of the liquid bridge with our IR camera because we do not have the optical properties for the test liquid. It is remarked that the optical properties of the 10-cSt silicone oil were finely measured [94]. The 10-cSt silicone oil is almost transparent against the light of 9 μm , 12 μm , 13 μm , and 14 μm in wavelengths, but not for 8 μm , 10 μm , and 11 μm . The absorption coefficients α [m^{-1}] for latter wavelengths are of 5.4×10^4 , 1.8×10^5 , and 3.3×10^4 , respectively. Hence, the intensities of the light at these wavelengths become $1/e$ of the original value in about 9 μm , 5.6 μm , and 30 μm . Suppose the silicone oil of 2cSt exhibits a similar characteristic in the transparency to that of 10cSt, the temperature detected by the IR camera apparently corresponds to the surface temperature. For the sake of brevity, we refer to these data as surface temperature.

We obtain the particle images with two synchronized high-speed complementary metal-oxide semiconductor (CMOS) cameras of 2048×2048 pixels (FASTCAM-Mini WX100, Photron, Inc., Japan). The frame rate of these cameras is set at 500 fps. One of the cameras is installed vertically above the top rod (HS-1 in the figure), and another one is installed horizontally aside the liquid bridge (HS-2). The top-view and side-view cameras capture the particle images through the top rod and the external shield, respectively. The image of the liquid bridge via the side-view camera

is also used to evaluate V/V_0 as well as Γ . To evaluate V , we detect the free-surface positions of the liquid bridge along each horizontal pixel at different height of the image. We stack vertically the slices of the liquid bridge of a pixel height under the assumption that each slice is a cylinder whose diameter corresponds to the distance between the positions of the detected free surfaces. It was confirmed that the free surface deforms within a range of $\pm 2 \mu\text{m}$ for the liquid bridge of $\Gamma = 2.0$ and $V/V_0 \sim 1.0$ with $R = 5 \text{ mm}$ under microgravity condition [54], and ranges $\pm 0.5 \mu\text{m}$ for $\Gamma = 0.64$ and $V/V_0 \sim 1.0$ with $R = 2.5 \text{ mm}$ under the normal gravity condition [67]. Thus the dynamic deformation of the liquid bridge is rather negligible in the present system.

As conducted in previous research [59,66,67,89], the particle positions against the traveling-wave-type thermal-flow field are reconstructed in the rotating frame of reference as follows: We obtain simultaneously the particle images by the top-view and side-view CMOS cameras with a light source (LLBK1-BA-15x15W, AI Tec System Co., Ltd., Japan) for whole illumination and the surface temperature images by the IR camera. The IR camera is placed at the position of $\pi/2$ apart from the side-view camera. The fundamental frequencies of the PAS and the surface temperature deviation are evaluated independently from both data by the top-view camera and the IR camera. The fundamental frequency of the oscillatory convection is constant during the period of the observation under the present conditions. Thus, the difference of phase among the data obtained by the top-view and the side-view CMOS cameras and the IR camera is constant. Because the fundamental frequencies of the rotating motion of the PAS and that of the traveling wave of the thermal-flow field are identical for $m = 1$ [59,60] as well as for $m = 3$ [55,66–68], the synchronization between the data by the high-speed CMOS cameras and the IR camera is achieved by delaying the phase of the data by the IR camera based on the period for the PAS to take in rotating azimuthally in $\pm\pi/2$ rad. The sign of the rotation angle is determined by monitoring the azimuthal direction of the PAS rotation. The particle images in the rotating frame of reference are obtained by accumulating the images after the rotation following the traveling-wave-type convection by the HTW instability [65,67]. In this case, the particle image in the rotating frame of reference is created by rotating the particle image at $t = t_0 + \Delta t$ around the origin \mathbf{O} with an angle of $-\omega_{\text{HTW}} \Delta t$, with the particle image at $t = t_0$ serving as the reference. Here, ω_{HTW} is the angular velocity of the TW-type convective structure caused by HTW instability.

In this paper, the target geometry on which we focus is the liquid bridge of $\Gamma = 1.6$ and $V/V_0 \sim 0.98 \pm 0.01$, respectively. We set the position of the end surface of the bottom rod at $z = 0 \text{ mm}$, thus the end surface of the top rod is located at $z = H = 1.2 \text{ mm}$. We vary $\Delta T = T_{\text{H}} - T_{\text{C}}$ from 35 K to 45 K (corresponding Ma from 2.9×10^4 to 3.9×10^4). It is confirmed in the preliminary experiments that the PAS without spiral in the HTW of $m_{\text{HTW}} = 1$ steadily emerges under ΔT from 40 K to 42 K or under corresponding Ma from 3.3×10^4 to 3.6×10^4 .

III. RESULTS AND DISCUSSION

Figure 2 shows a typical example of the time series of the particle images of the PAS under $\Delta T = 40 \text{ K}$ or $\text{Ma} = 3.3 \times 10^4$ obtained through the present study. Figures 2(a) and 2(b) illustrate the particle images observed through the top rod (top-view images), and Fig. 2(c) illustrates those observed through the external shield (side-view images). The particle images shown in Fig. 2(b) are the same as those in Fig. 2(a), but with indices to follow some typical particles (particle b_1 , b_2 , and a). Note that the top-view images are indicated after the inversion of the grey scale for the sake of visibility. The particles appear in black for both the top-view and side-view inverted images. The particles gather to align, forming a closed structure PAS of $m = 1$ about the z axis of the liquid bridge. The PAS seems rotating without changing its shape or spatial structure at a constant azimuthal angular velocity. In this example, the rotating direction of the PAS is counterclockwise when one observes from above. The PAS locates in the vicinity of the free surface and never penetrates into the deep interior region of the liquid bridge. It is emphasized that this PAS does not consist of a spiral structure in the interior region, which has been demonstrated by experiments [59,60,85] and numerical simulations [87,88]: The present coherent structure exhibits a closed path

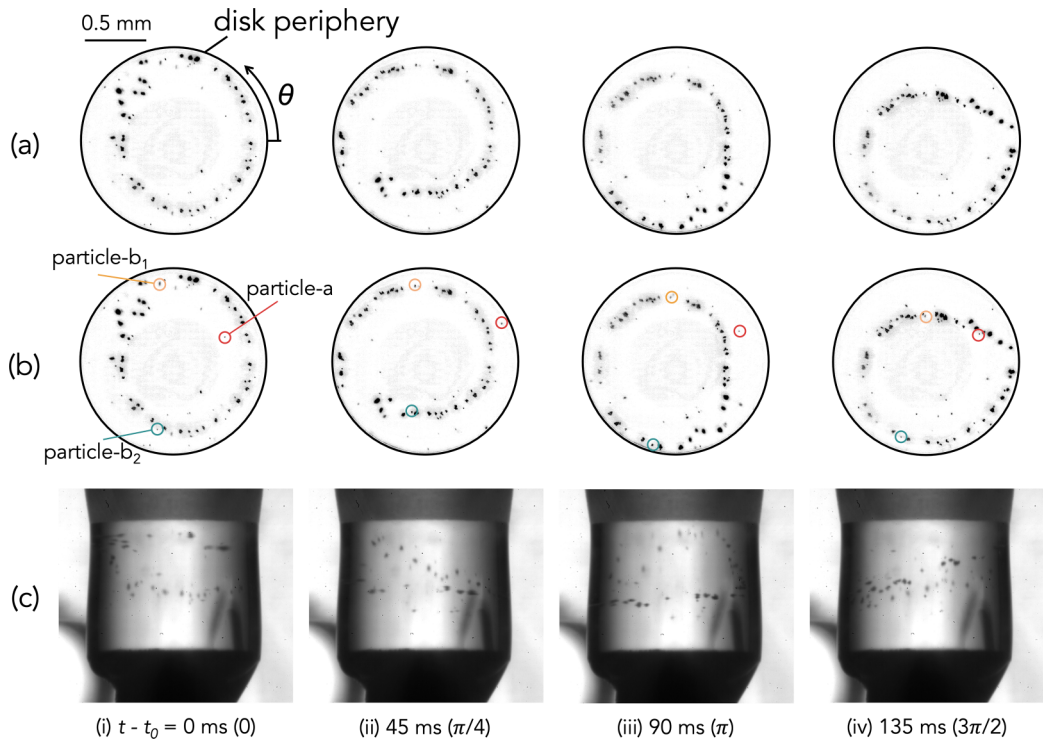


FIG. 2. Typical example of time series of particle images of PAS under $\Delta T = 40$ K or $\text{Ma} = 3.3 \times 10^4$: (a), (b) Particle images observed through the upper rod (top-view images), and (c) those observed through the external shield (side-view images). The particle images shown in (b) are the same as those in (a); we put indices in (b) to follow some specific particles (particles b_1 , b_2 , and a).

in 2π in the azimuthal direction without exhibiting a helical motion in the returning flow near the bottom rod toward the top rod. Such PAS is named in the present paper as the PAS without a spiral in the HTW of $m = 1$. The particles b_1 and b_2 keep forming this type of PAS; these are chosen as typical examples of the majority of the suspended particles to form this type of PAS. Particle a, on the contrary, travels in the vicinity of the coherent structure by the major group of the particles to which particles b_j belong. The characteristics of particles b_1 , b_2 , and a will be discussed in Fig. 3. Note again that the side views of the particle images are detected via the high-speed CMOS camera located at $\theta = 0$ rad. The particles forming this coherent structure, such as the particles b_j , travel clockwise, i.e., in the opposite direction to the PAS. This is a common feature for the PASs with a spiral in the HTW of $m = 1$ [59,60] as well as those for the PASs of $m = 3$ [55,62,63,66–68,95]. The fundamental frequency of the PAS rotation in the azimuthal direction is evaluated as $f_{\text{HTW}} = 5.58$ Hz by analyzing the top-view particle images. Under the present conditions, it is confirmed that $\tau_{\text{PAS}} = \tau_{\text{HTW}}$, as measured in the case of $m = 3$ [67,68]. Thanks to the condition $V/V_0 \sim 1$, the curvature of the free surface along the z axis becomes smaller than that in the liquid bridges of $V/V_0 < 1$ as employed in Refs. [59,60]. Such a liquid-bridge shape enables us to track the particles in the side-view images especially at $\theta \sim 0$, where the side-view camera is installed, and the opposite side (at $\theta \sim \pi$). By comparing of the azimuthal positions of the particles obtained in the top-view images, we determine the height positions of the corresponding particles. Figures 3(a) and 3(b) illustrate the time series of the particles as labeled in Fig. 2(b) as b_1 [in column (i)], b_2 [in column (ii)], and a [in column (iii)]: Rows (a) and (b) in Fig. 3 indicate the particles' motion in the laboratory frame and in the rotating frame of reference, respectively. Particles b_1 and b_2 belong to

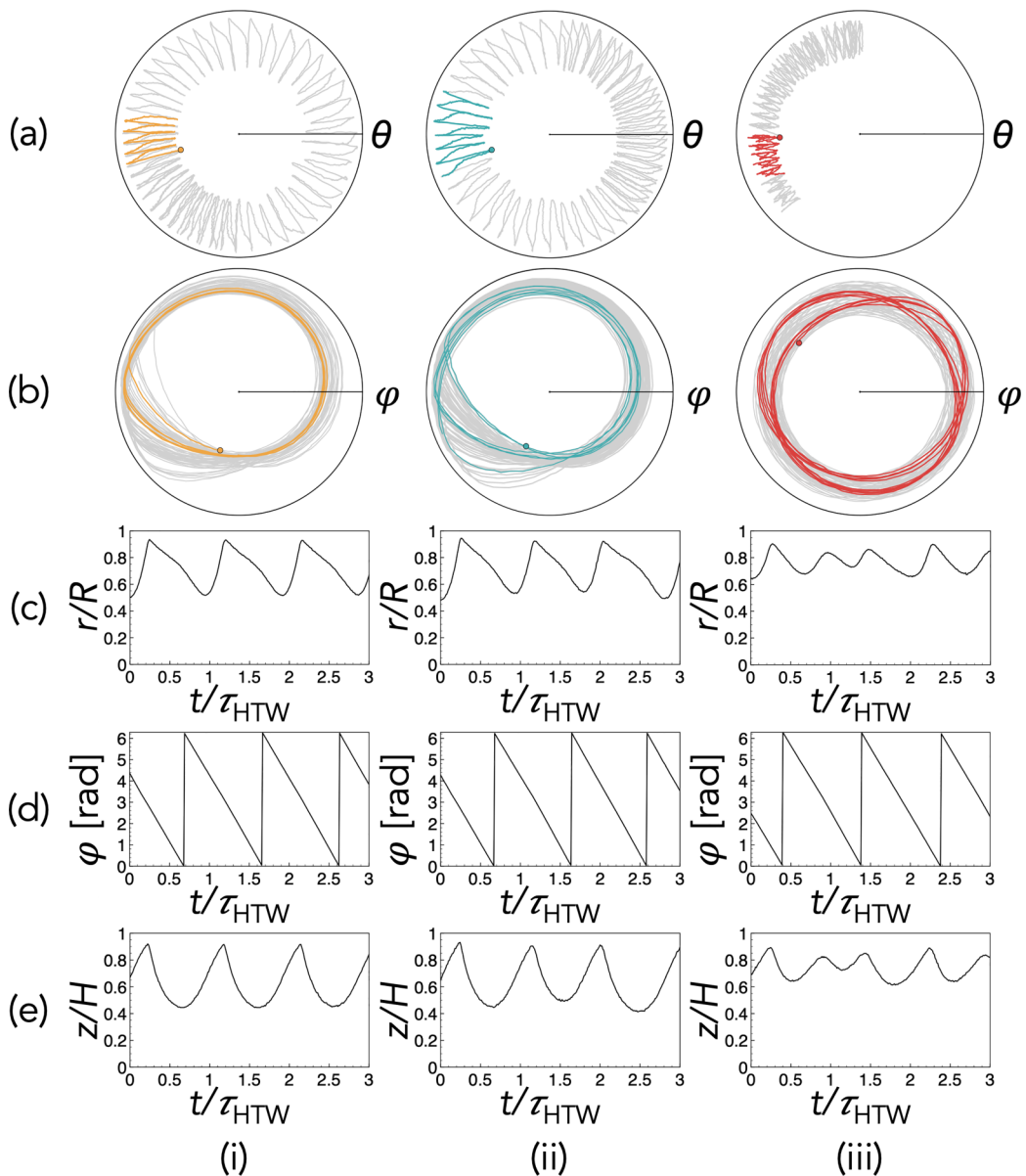


FIG. 3. (a), (b) Time series of projected trajectories of particles labeled b_1 [in column (i)], b_2 [in column (ii)], and a [in column (iii)] in the laboratory frame and in the rotating frame of reference, respectively. Each label is the same as illustrated in Fig. 2(b). The trajectories in grey are the whole data detected within a period of 10.914 s or 60.91 period of the PAS rotation. The colored trajectory in each frame indicates mimicked data for $\Delta\tau = 0.860$ s for particle b_1 , 1.062 s for particle b_2 , and 1.786 s for the particle a . A small circle is plotted in each frame to indicate $\tau/\tau_{HTW} = 0$ of the particle within the mimicked period, which corresponds to the position of r_{\min} nearest to the beginning of the tracked particle trajectory. (c)–(e) Time series of the radial (r/R), azimuthal (φ), and axial (z/H) positions of each particle, respectively.

the particle group forming the PAS without a spiral in the HTW of $m = 1$ as indicated. Particle a travels near the PAS, but does not belong to the group to form the PAS to which particles b_j belong. The trajectories in grey are the whole data detected within a period of 10.914 s or 60.91 period of the PAS rotation. The colored trajectory in each frame indicates a mimicked data for $\Delta\tau = 0.860$ s (corresponding to a period of the PAS rotation $\Delta\tau/\tau_{\text{PAS}} = \Delta\tau/\tau_{\text{HTW}} = 4.80$) for particle b_1 , for 1.062 s (5.93), for particle b_2 , and for 1.786 s (9.97) for particle a . The orbits of these particles appear to be almost periodic. This is largely due to the fact that the colored regions are very short term and the orbits are long-term nonperiodic (gray-colored regions). A small circle is plotted in each frame to indicate $\tau/\tau_{\text{HTW}} = 0$ of the particle within the mimicked period. We start tracking these particles when their radial position is minimum or $r = r_{\text{min}}$. In the laboratory frame (Panel (a) in Fig. 3), the particles b_j travel azimuthally in clockwise as previously stated. In the rotating frame of reference (Panel (b) in Fig. 3), the particles travel toward the free surface from the interior region of the liquid bridge, and then they travel near the free surface by sliding down toward the bottom rod, whereupon they return in the interior region without exhibiting a helical motion as observed in the terrestrial and microgravity experiments [59,60] as remarked. The particles travel to form the PAS not along a fixed linelike trajectory, but along the trajectories scattered in a limited region. While the flow under a fixed Ma is apparently steady and periodic in φ in the rotating frame, the trajectories of the marked particles on their respective PAS are not exactly periodic. This may indicate that they move in the vicinity of KAM tori which are nested around periodic streamlines. It would not be able to definitively determine, unfortunately, whether the streamlines and KAM tori are actually spatially periodic in our experiments. After changing their direction near the free surface, the particles follow a narrow region to form the PAS without a spiral. That is, the trajectory periodically returns close to itself near the free surface. We also find another type of PAS: Particle a is a particle traveling temporarily in the vicinity of the PAS of $m = 1$ without a spiral. In the laboratory frame, this particle travels counterclockwise in the azimuthal direction, i.e., the same direction as the rotation of the PAS without a spiral. This is a unique feature of this particle a . In the case of the PAS of $m = 3$, a similar feature is sometimes seen for the particles forming the core [55,68]. It must be noted that the particles forming the core exhibit rather random motion [22]; they move back and forth in the azimuthal direction [68]. Particle a , on the contrary, keeps traveling in the same azimuthal direction in net: Notwithstanding that particle a sometimes travels clockwise for a while within a period for its turnover motion, this particle moves counterclockwise after each turnover period as illustrated in frame (iii)-(a) in Fig. 3. Such azimuthal motion in net of the particles was detected for the PAS in the HTW of $m = 1$ with a spiral [59,60], but not for the particles on the core [68]. In the rotating frame of reference, this particle a is found to exhibit another type of the ordered trajectory in a short period. In other words, this particle is attracted to a different periodic attractor (or limit cycle). It closes after twofold revolutions in the azimuthal direction. It is found that the trajectories by particles b_j and a are quite similar to the structures labeled as groups B and A, respectively, by Barmak *et al.* [92]: We thus label these particles as b_j and a . It is also emphasized that particles b_j travel, whose trajectory is rather scattered within a tubular region of a finite cross area, whereas particle a travels along a quite narrow region as if the particle travels for a while along a line-like trajectory.

The monitored particle trajectories may seem periodic on a short timescale, with a period of one to close the structure for particles b_j and with a period of two for particle a (as shown by the colored parts of the trajectories in Fig. 3). On a longer timescale, the trajectories are not periodic. Notwithstanding, each long-term trajectory always stays within a thin torus of period one in φ . This may imply that attractors, which could be slightly chaotic, exist. It is noteworthy that these toroidal regions to which the particles are attracted are quite similar to the KAM tori discovered by Barmak *et al.* [92]. Further discussion will be made by illustrating the Poincaré sections (Figs. 7 and 8).

Figures 3(c)–3(e) illustrate the time series of the reconstructed positions of the particles as shown in rows (a), (b): each row indicates the radial (r/R), azimuthal (φ), and axial (z/H) positions, respectively, for particles (i) b_1 , (ii) b_2 , and (iii) a . These graphs indicate their variations in a threefold period of the PAS rotation or $0 \leq t/\tau_{\text{HTW}} \leq 3$. Note that Fig. 3(d) indicates the azimuthal position in the rotating frame of reference. One finds that Fig. 3(c), the radial position of particle

b_j , exhibits a single maximum in a single period of the PAS rotation. This differs from the cases of the particle forming the PAS with a spiral in the HTW of $m = 1$ by Refs. [59,60,85], in which the radial position exhibits double maxima in a single period. After particles b_j reach closest to the free surface, or $r = r_{\max}$, it gradually penetrates into the interior region of the liquid bridge and reaches the minimum position. Such minimum position, r_{\min} , corresponds to the minimum radial position of the trajectory of a particle on the attractor. The variation of (d), the azimuthal behavior in the rotating frame of reference, seems almost constant; the temporal variation of φ is almost completely dominated by the azimuthal velocity of the rotating frame of reference. When one pays attention to the variation in z , particles b_j keep traveling in the top-half of the liquid bridge; the particles do not go further down in the bottom half. Particle a, on the contrary, (c) the variation of the radial position becomes different from that of the particles b_j ; there exist three maxima in the twofold periods of the PAS rotation. This ordered trajectory exists within a more limited region in z ($0.6 \lesssim Z/H \lesssim 0.9$) than that by the particles b_j . For both of the particles b_j and a, the radial and axial positions become locally maximum at the same instant for each despite the difference in their structures. That is, the orbit for both types of the PASs reach locally highest in z when they come closest to the free surface in r . It is also found that the maximum radial and axial positions (r_{\max} and z_{\max}) for particles b_j are larger than those for the particle a, and the minimum ones for the particles b_j are smaller than those for the particle a. It must be indicated that quite a few particles are found to exhibit an ordered trajectory similar to that by particle a in the present series of experiments: Another attractor with the shape of type A does coexist with type B in the liquid bridge, but there exists a notable difference in the number of particles attracted by two distinct type of PASs. This may imply that the attractor of the PAS of Type B is quite stably strong to attract many particles in the liquid bridge, whereas type A is very weak or unstable. What we find through the present series of experiments are there exist (a) nonperiodic (but almost periodic) trajectories such that a kind of fuzzy PAS results with period one on average (particles b_j) and (b) almost periodic PAS with period two on the short timescale (particle a). It is unclear yet for the latter if period two can be resolved on the long timescale. It is remarked that the particles are attracted to either one of two attractors. The identified attractors are not simply periodic; it could possibly be that the attractors have a high periodicity. These highly periodic attractors are hypothesized to be in close proximity to KAM structures that possess a high period in φ , as described by Barmak *et al.* [92]. Alternatively, the attractors may exhibit weakly chaotic behavior and may be located near regular KAM structures. Note that the difference between a periodic attractor with very high periodicity and a chaotic attractor may not be resolvable, even numerically (e.g., see Ref. [79]).

Our finding leads to what formerly has been called ‘‘PAS with a spiral’’ [59] by a phenomenological terminology is in fact a subharmonic PAS with period two in the HTW with a wave number $m = 1$. That is, we experimentally find another period-two PAS, the PAS without a spiral that closes after twofold revolutions (type A), which is different from the PAS with a spiral structure in the interior region of the liquid bridge [59,60]. Figure 4 illustrates the particle trajectories in the top-view images in the laboratory frame that we succeed in reconstructing the time series of their three-dimensional positions. We label the partially reconstructed trajectories of particle b_1 as $B_1^{(1)}$ for $2.108 \text{ s} \leq t \leq 2.968 \text{ s}$ (for $\Delta t = 0.860 \text{ s}$) and $B_1^{(2)}$ for $5.342 \text{ s} \leq t \leq 7.452 \text{ s}$ (for $\Delta t = 2.112 \text{ s}$), and those of particle b_2 as $B_2^{(1)}$ for $1.966 \text{ s} \leq t \leq 3.386 \text{ s}$ (for $\Delta t = 1.422 \text{ s}$) and $B_2^{(2)}$ for $5.508 \text{ s} \leq t \leq 6.570 \text{ s}$ (for $\Delta t = 1.062 \text{ s}$). We also label particle a as trajectory $A^{(1)}$ for $7.470 \text{ s} \leq t \leq 9.256 \text{ s}$ (for $\Delta t = 1.786 \text{ s}$). Note again that we succeed in detecting the z position of the particles when the particles travel in the limited regions of $\theta \sim 0$ and π as stated: The side-view camera is installed at $\theta = 0$ in the laboratory frame. Because of the small-sized liquid bridge to overcome inevitable deformation due to the static pressure, the common fields of view by the top-view and side-view cameras to track the particles are quite limited compared to the liquid bridges formed under microgravity conditions [48,49]. Especially due to the small radius of the liquid bridge, the refraction at the free surface becomes more significant. That is the reason we reconstruct the three-dimensional positions of the particles within regions limited in the azimuthal direction as illustrated.

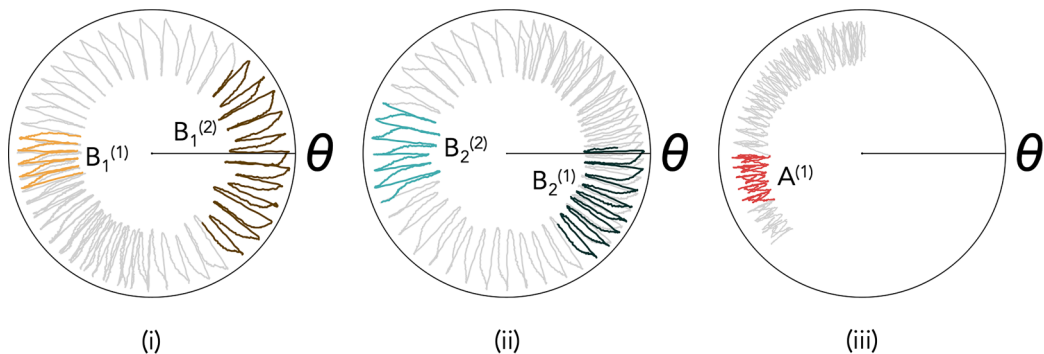


FIG. 4. Trajectories in laboratory frame succeeded in three-dimensional reconstruction from data of (i) particle b_1 , (ii) particle b_2 , and (iii) particle a superimposed upon whole trajectories in grey (as shown in Fig. 3).

To distinguish the particle behaviors to form coherent structures, we evaluate the frequency ratio of the particle turnover motion, $f_p = 1/\tau_p$, to the traveling-wave-type convection caused by the HTW instability, $f_{HTW} = 1/\tau_{HTW}$ [67]. The frequency of the particle turnover motion is evaluated by measuring the inverse of the period between r_{min} 's as illustrated in Fig. 3. The frequency of the HTW is evaluated from the rotation of the PAS observed by the top-view camera as aforementioned. Note that the rotation period τ_{HTW} remains constant under the corresponding Ma. The frequency ratio f_p/f_{HTW} for $B_1^{(1)}$, $B_1^{(2)}$, $B_2^{(1)}$, and $B_2^{(2)}$ are of 0.967, 0.972, 0.977, and 0.971, respectively, whereas that for $A^{(1)}$ is of 0.668. That is, the particles on the PAS of type B have almost period one, and the particle on the PAS of type A has almost period two (or threefold overturns within two periods yield $0.668 \times (3/2) \sim 1$). It is confirmed that f_p/f_{HTW} remains almost constant for $B_j^{(i)}$ notwithstanding the variations in the trajectories. Additionally, it is observed that the particles associated with the trajectories $B_j^{(i)}$ and $A^{(1)}$ exhibit different structures in the thermal-flow field. Figure 5 indicates (a) the bird's-eye views and (b) the top views of the reconstructed trajectories for a certain period by (1) particles b_j and (2) particle a . The reconstructed regions are the same as defined in Fig. 4. One finds the plane of $\varphi = 0$ in both bird's-eye and top views to facilitate comparison of the positions of

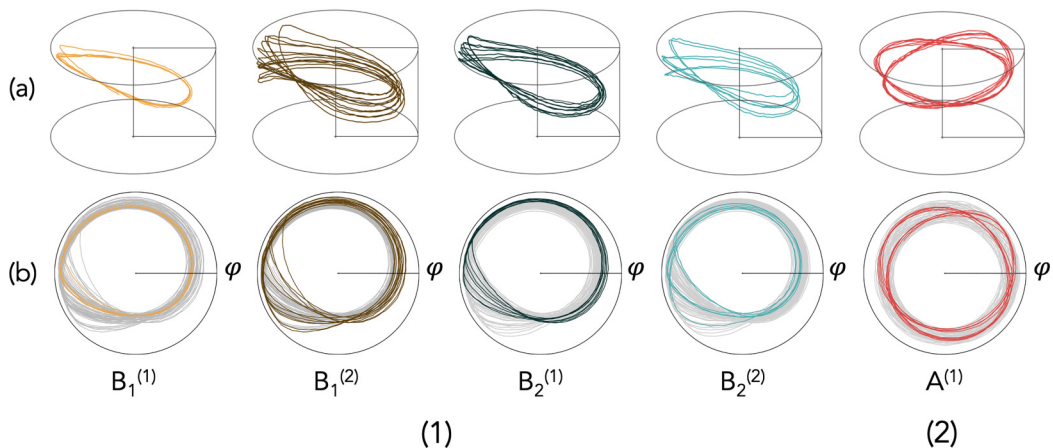


FIG. 5. Reconstructed trajectories of (1) particles b_j and (2) particle a in (a) bird's-eye views and (b) top views. The reconstructed regions are the same as defined in Fig. 4. Note that the whole data of the trajectories in (b) the top views are illustrated in grey.

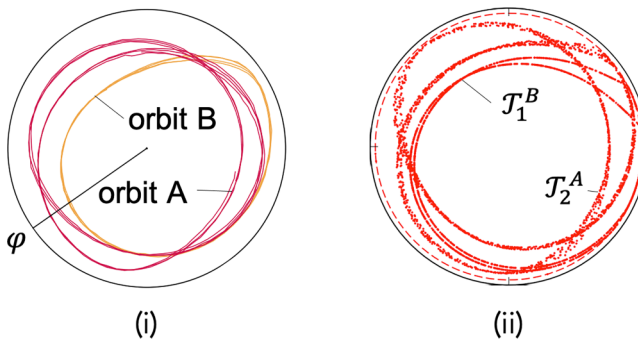


FIG. 6. Comparison between (i) particle trajectories obtained in the present study and (ii) coherent structures predicted by Barmak *et al.* [92]: Panel (i) consists of the trajectories by the particle b_1 and a , which are labeled orbit B and orbit A, respectively. The conditions for both experimental and numerical results are as follows: (i) $\varrho = 2.36$, $\Gamma = 1.6$, $\text{Pr} = 28.6$, $\text{Re} = 1.42 \times 10^3$, and $\text{St} = 9.7 \times 10^{-6}$ and (ii) $\varrho = 2$, $\Gamma = 1$, $\text{Pr} = 68$, $\text{Re} = 1500$, and $\text{St} = 7.606 \times 10^{-5}$.

the particle trajectories. The trajectories $B_j^{(i)}$ and 'A⁽¹⁾' have different three dimensional structures. We imply that the trajectory of the particles does not always remain as sharp as linelike structures but scatters during the observation period: In focusing on the particle b_1 , for instance, this particle travels regularly, whose path exhibits a sharp linelike orbit without scatter in the early stage of the observation, labeled $B_1^{(1)}$. In the later stage, labeled $B_1^{(2)}$, on the contrary, the trajectory lies broader in r and z despite that the trajectory apparently exhibits a spatial structure of the PAS of $m = 1$ without a spiral. The trajectory does not return to the same (r, z) location for constant φ , then the Poincaré points would scatter. The trajectory labeled $B_2^{(1)}$ for particle b_2 , whose observation period is almost the same as $B_1^{(1)}$, the trajectory locates in rather the outer rim of the trajectory distribution. Therefore, within this observation period, the particle is not attracted to a perfectly periodic orbit. The period being slightly less than that of the HTW (deviation is about 3%). Such features are also detected in relation to $B_1^{(2)}$ and $B_2^{(2)}$, which are observed at approximately the same time period. From these results, the scatter of linelike trajectories of particles b_1 and b_2 are explained by considering the KAM tori [92]: The KAM torus is a closed stream tube on which a regular streamline winds. The spatial structure of the trajectories of $B_j^{(i)}$ are similar to the torus \mathcal{T}_1^B . When one pays attention to particle a , on the other hand, this particle temporarily forms a linelike structure. This particle keeps traveling along an orbit, and the trajectory overlaps densely. For the period-two orbit, the deviation is only about 0.2%, which may signal the periodicity. The spatial structure of this trajectory is quite similar to the closed streamline labeled \mathcal{L}_2^A . Figure 6 indicates a comparison between (i) the particle trajectories obtained in the present study and (ii) the coherent structures predicted by Barmak *et al.* [92]: Panel (i) consists of the partial trajectories by the particles b_1 and a , which are labeled orbit B and orbit A, respectively. Panel (ii) consists of the coherent structures by the particles whose spatial structure resembles the KAM torus labeled as \mathcal{T}_1^B and the closed streamline labeled as \mathcal{T}_2^A [92]. The subscript indicates the number of the revolution about the z axis for the particle to close their trajectory. The conditions for both experimental and numerical results are as follows: (i) $\varrho = 2.52$, $\Gamma = 1.6$, $\text{Re} = 1.42 \times 10^3$, and $\text{St} = 9.7 \times 10^{-6}$ and (ii) $\varrho = 2$, $\Gamma = 1$, $\text{Re} = 1500$, and $\text{St} = 7.606 \times 10^{-5}$. Both orbits A and B, as well as the HTW, rotate with the same angular velocity in the laboratory frame. Consequently, the azimuthal phase difference between orbits A and B is constant. That is, one would find these two structures rigidly rotate without changing their mutual positions in the laboratory frame. This panel reveals through the present experiments that there exist two different attractors simultaneously in the liquid bridge. Notwithstanding the differences in Γ and in the thermal property in terms of Pr between the present experiment and the numerical simulation [92], the shapes of different orbits and their

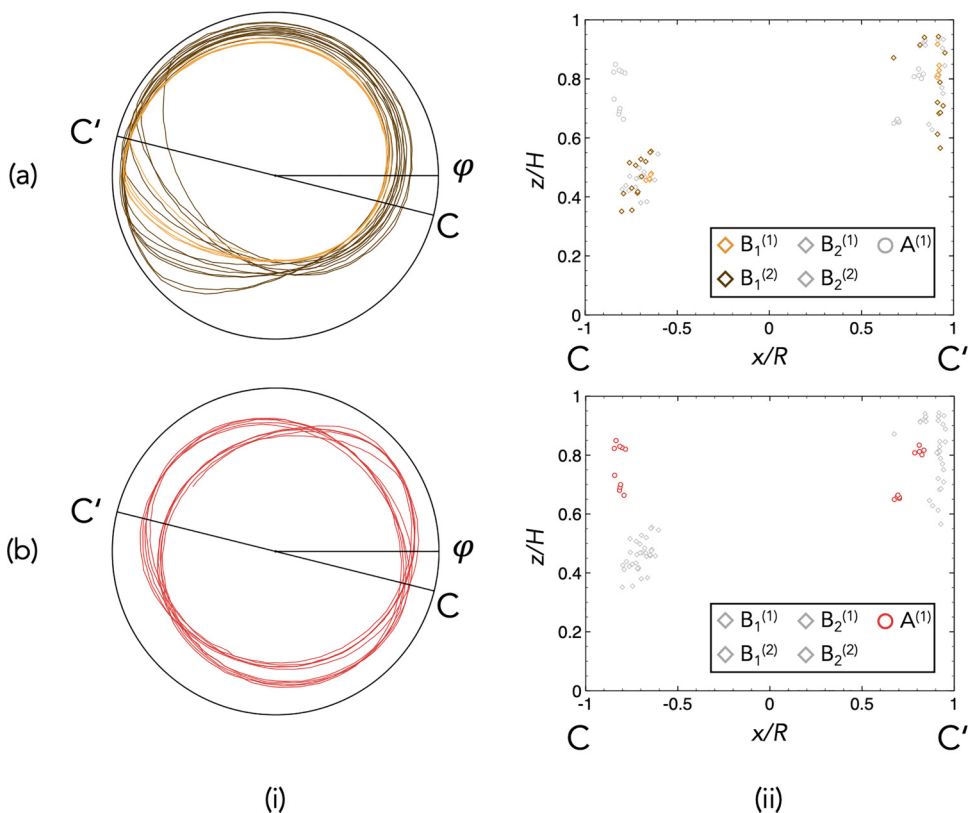


FIG. 7. Column (i): Top view of trajectories of (a) particle b_1 and (b) particle a . Column (ii) Poincaré section at C-C' cross section shown in column (i). Row (a) consists of the trajectories (a) $B_1^{(1)}$ (in orange) and $B_1^{(2)}$ (in brown) by particle b_1 , and row (b) consists of trajectory $A^{(1)}$. Corresponding Poincaré points in column (ii) are plotted in the same color as in column (i). The Poincaré points by different particles are illustrated in grey in each frame.

mutual spatial correlation show a significant agreement in quality. It is emphasized that Barmak *et al.* [92] predicted that the accumulation of the particles depends on ϱ : For smaller ϱ ($\varrho \leq 1.5$ in their case), the PAS that closed after twofold revolutions about the z axis, or group A, would be dominantly formed. For larger one ($\varrho = 2$ in their case), the two types of PASs, the groups A and B, would coexist. The present experimental results clearly indicate the coexistence of the PASs of $m = 1$ with the particles of $\varrho = 2.36$; the one without a spiral, and the other that closed after the twofold revolutions about the z axis. For coherent structures of $m = 3$, previous research [65,67,68] has indicated that the coherent structures by low St-number particles are highly correlated with the KAM tori. This leads us to consider that the KAM tori would be formed in the present system as well, whose spatial structures are similar to the PAS of type B (without a spiral) and type A (whose trajectory closes after the twofold revolutions). In the following, a comparison is made from a different perspective using Poincaré sections of the reconstructed particle trajectories. Figure 7 indicates (i) the top view of the trajectories by (a) particle b_1 and (b) particle a in the rotating frame of reference, and (ii) the Poincaré section at C-C' cross section as shown in column (i). Note that the azimuthal position to illustrate the Poincaré section is determined by almost following Barmak *et al.* [92]. They defined the position $\varphi = 0$ where the surface temperature becomes maximum, and the Poincaré section was obtained on the full plane $\varphi = -\pi/4$ and $\varphi = 3\pi/4$, while in the present study it is quite difficult to measure the surface temperature precisely via the IR camera. We

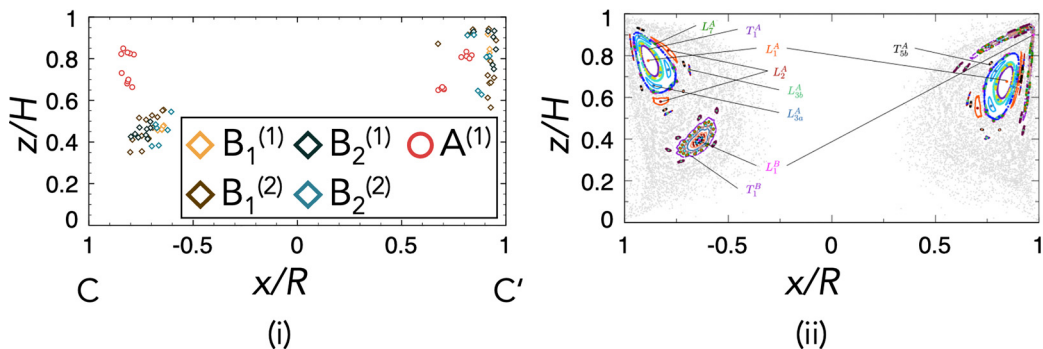


FIG. 8. Comparison of Poincaré sections (i) by present paper and (ii) of streamline topology predicted by Barmak *et al.* [92]. Panel (i) consists of the all data for the trajectories $B_j^{(i)}$ and a as separately illustrated in Fig. 7 (redrawn in the rescaled graph to correspond to panel (ii)). The conditions for both experimental and numerical results are as follows: (i) $\Gamma = 1.6$, $\text{Re} = 1.42 \times 10^3$ and (ii) $\Gamma = 1$, $\text{Re} = 1500$.

then adopt the cross section passing the intersection position of particle trajectory $A^{(1)}$ as shown in Figs. 7(i)–7(b) as a reference. The present results illustrated in this figure indicate that the Poincaré points by particles b_j and a distribute in quite different manner, whereas there exist two major regions where the Poincaré points locate in common. For particles b_j , the Poincaré points mainly distribute obliquely to the central axis of the liquid bridge: In the region of $x/R > 0$, they are dispersed in a flipped L shape in the region $0.5 < z/H < 0.9$, while in the region of $x/R < 0$ they distribute relatively dense in the region $0.4 < z/H < 0.6$. This is a characteristic feature of orbit B. When one tracks the Poincaré points of particles b_j on the cross section, the position of the points varies in each passing event at different instances. They distribute over a wider region in the trajectories $B_j^{(2)}$ (in the latter half of the time series) than in the trajectories $B_j^{(1)}$ (in the first half of the time series) as discussed in Fig. 5. For particle a, on the contrary, the Poincaré points are densely distributed in separated regions in the top-half of the liquid bridge. Furthermore, there are two dense distributions in each for both $x/R > 0$ and $x/R < 0$. When one tracks the Poincaré points of the trajectory $A^{(1)}$ (by particle a), the point appears alternately in one of the two fixed regions in each of the r - z planes in $x/R > 0$ and $x/R < 0$. This corresponds to the spatial structure of this PAS that closes after the twofold revolutions about the z axis. This is a characteristic feature of orbit A. It is noted again that this trajectory is found in the latter half of the time-series data: The ordered structure A is found to emerge in the latter half period of the observation, in which the rather scattered trajectories $B_j^{(2)}$ are observed. We do not have reach comprehensive conclusion about the variation of the trajectories as a function of time; such variation be caused whether the ordered regions of the thermal-flow field (the KAM tori) themselves are spatiotemporally unstable under this condition or the KAM tori are stably formed but the particles are not stably attracted to keep traveling in these regions. For further discussion, it is indispensable to establish an experimental system that allows us to measure the particle behavior more accurately over extended durations.

Comparison of the Poincaré sections (i) by the present paper and (ii) of the streamline topology predicted by Barmak *et al.* [92] is made in Fig. 8. Panel (i) consists of the all data as separately illustrated in Fig. 7. Note that the aspect ratio of the graph is modified to match that by Barmak *et al.* [92]. The conditions for (ii) the numerical simulation are the same as introduced for Fig. 6. The Poincaré points by the trajectories $B_j^{(i)}$ distribute closer to the free surface than those by trajectory $A^{(1)}$ in the cross section of $x/R > 0$, and vice versa in the cross section of $x/R < 0$. For trajectory $A^{(1)}$, the Poincaré points form four dense groups as previously stated. It is noted anew there exist unavoidable differences between the present experiments and the numerical analysis in terms of the liquid bridge geometry (Γ and V/V_0), the liquid properties (Pr, the temperature dependence of the properties and the evaporation of the test liquid), as well as the experimental conditions in

Re and heat transfer between the liquid bridge and the surrounding gas, and so on. Despite such discrepancies in the conditions, the present results demonstrate at least two different attractors with different periods coexisting in the HTW of $m = 1$, and these attractors seem to be related to two different sets of KAM tori which are analogous to the tori \mathcal{T}_1^B and \mathcal{T}_2^A for a similar (but different) high-Prandtl-number liquid bridge.

Under normal gravity conditions, it is quite intractable to conduct experiments by employing the high-Pr liquids as Barmak *et al.* [92] adopted. Fine experiments under microgravity conditions with large-scale liquid bridges, as demonstrated by Sakata *et al.* [59], would be invaluable in achieving comprehensive understanding of such unique phenomenon through more direct comparisons.

IV. CONCLUDING REMARKS

We investigate experimentally coherent structures of low-Stokes-number particles driven by the thermocapillary effect in a closed system. The target geometry is a high-aspect-ratio half-zone liquid bridge, where the PAS [19] in the thermal-flow fields of $m = 1$ in azimuthal wave number emerges. To aim at minimizing deviations of the shape of the liquid bridge from cylindrical, which is caused by the static pressure difference between liquid and gas under the normal gravity condition, a small-scale liquid bridge of $O(10^{-3} \text{ m})$ is adopted.

We discover the PAS in the HTW of $m = 1$, whose spatial structure is different from those indicated by the previous terrestrial [59,60,85] and microgravity [59] experiments, and by the numerical simulations [87,88], with the particles heavier than the test liquid. This is the unveiling of another type of PAS that has only been predicted by numerical simulation [90–92]. The coherent structures by the particles are illustrated in the laboratory frame and in the rotating frame of reference. Their spatial structure is formed to close after a single revolution about the z axis, and is similar to that predicted by Barmak *et al.* [92], which is named in the present paper as the PAS without a spiral in the HTW of $m = 1$. Individual particles of $St = O(10^{-5})$ are tracked to indicate their spatial-temporal behaviors forming the coherent structures. We indicate that two major trajectories are simultaneously emanated inside the liquid bridge of $\Gamma = 1.6$: One is closed after a single revolution about the z axis (with a period of one), and the other is closed after the twofold revolutions about the z axis (with a period of two) without penetrating into the interior region of the liquid bridge as predicted by Barmak *et al.* [92]. We demonstrate that the present thermocapillary driven convection is characterized by multiple solutions due to the coexistence of closed streamtubes with different spatial structures in the rotating reference system. Depending on the specific conditions considered, particles may be attracted by one or even two ordered flow structures.

We succeed in tracking some particles not only in the two-dimensional system with the projected view observed from above but also in the three-dimensional system by the simultaneous monitoring the suspended particles by two synchronized high-speed cameras from different view angles. The Poincaré sections are successfully illustrated to indicate the spatial correlation between the ordered trajectories. We indicate that the particle trajectory does not always locate within a finely narrow area as a linelike structure but especially scatters the region for the particles travel near the heated rod toward the free surface on a long-time scale. We have not reached any conclusions whether the scatter of the trajectory is caused by the experimental imperfection or reflect the phenomenon itself. It is noteworthy, in the case of $m = 3$, that the KAM (\mathcal{T}_3^3) exhibits a rather flattened shape near the free surface [79,83]. The “stretching is caused by high strain rate . . . due to the large thermocapillary stresses near the hot corner” (for the case of $m = 1$) [92]. The scatter of the trajectory near the free surface, as observed in the present series of experiments, might be indicative of the shape of the KAM attracting the particles. The comparison of the Poincaré sections implies that the thermal-flow field inside the liquid bridge is almost identical, realized in the coherent structures, notwithstanding the differences in the geometry of the liquid bridge and the physical properties of the test liquid.

Further research would be inevitably needed to investigate the stability of the coherent structures with different periods and the corresponding thermal-flow field. Experimental approaches, such as

fine experiments by employing large-scale liquid bridges under microgravity conditions as Sakata *et al.* [59] conducted, would be necessary.

ACKNOWLEDGMENT

This work was partially supported from the Japan Society for the Promotion of Science (JSPS) by Grant-in-Aid for Challenging Research (Exploratory) (Grant No. 20K20977).

-
- [1] V. Mikol, J.-L. Rodeau, and R. Giegé, Experimental determination of water equilibration rates in the hanging drop method of protein crystallization, *Anal. Biochem.* **186**, 332 (1990).
 - [2] K. Provost and M.-C. Robert, Application of gel growth to hanging drop technique, *J. Cryst. Growth* **110**, 258 (1991).
 - [3] J. Jancarik and S.-H. Kim, Sparse matrix sampling: A screening method for crystallization of proteins, *J. Appl. Cryst.* **24**, 409 (1991).
 - [4] J. Day and A. McPherson, Macromolecular crystal growth experiments on international microgravity laboratory-1, *Protein Sci.* **1**, 1254 (1992).
 - [5] S. Koszelak, J. Day, C. Leja, R. Cudney, and A. McPherson, Protein and virus crystal growth on international microgravity laboratory-2, *Biophys. J.* **69**, 13 (1995).
 - [6] P. Sajeesh and A. K. Sen, Particle separation and sorting in microfluidic devices: a review, *Microfluidics Nanofluidics* **17**, 1 (2014).
 - [7] A. Yusa, M. Toneri, T. Masuda, S. Ito, S. Yamamoto, M. Okochi, N. Kondo, H. Iwata, Y. Yatabe, Y. Ichinosawa, S. Kinuta, E. Kondo, H. Honda, F. Arai, and H. Nakanishi, Development of a new rapid isolation device for circulating tumor cells (CTCs) using 3D palladium filter and its application for genetic analysis, *PLoS ONE* **9**, e88821 (2014).
 - [8] B. Behdani, S. Monjezi, M. J. Carey, C. G. Weldon, J. Zhang, C. Wang, and J. Park, Shape-based separation of micro-/nanoparticles in liquid phases, *Biomicrofluidics* **12**, 051503 (2018).
 - [9] H. Haddadi, H. Naghsh-Nilchi, and D. D. Carlo, Separation of cancer cells using vortical microfluidic flows, *Biomicrofluidics* **12**, 014112 (2018).
 - [10] O. Rouaud and M. Havet, Computation of the airflow in a pilot scale clean room using $k - \epsilon$ turbulence models, *Int. J. Refrig.* **25**, 351 (2002).
 - [11] M. J. Olascoaga and G. Haller, Forecasting sudden changes in environmental pollution patterns, *Proc. Natl. Acad. Sci. USA* **109**, 4738 (2012).
 - [12] J. A. Ivar do Sul and M. F. Costa, The present and future of microplastic pollution in the marine environment, *Environ. Pollut.* **185**, 352 (2014).
 - [13] K. Zhang, W. Gong, J. Lv, X. Xiong, and C. Wu, Accumulation of floating microplastics behind the three gorges dam, *Environ. Pollut.* **204**, 117 (2015).
 - [14] S. Sharma and S. Chatterjee, Microplastic pollution, a threat to marine ecosystem and human health: A short review, *Environ. Sci. Pollut. Res.* **24**, 21530 (2017).
 - [15] M. Sighicelli, L. Pietrelli, F. Lecce, V. Iannilli, M. Falconieri, L. Coscia, S. Di Vito, S. Nuglio, and G. Zampetti, Microplastic pollution in the surface waters of italian subalpine lakes, *Environ. Pollut.* **236**, 645 (2018).
 - [16] M. Rodrigues, N. Abrantes, F. Gonçalves, H. Nogueira, J. Marques, and A. Gonçalves, Spatial and temporal distribution of microplastics in water and sediments of a freshwater system (Antuã River, Portugal), *Sci. Total Environ.* **633**, 1549 (2018).
 - [17] S. Kadowaki, Size distribution of atmospheric total aerosols, sulfate, ammonium and nitrate particulates in the Nagoya area, *Atmos. Environ.* (1967) **10**, 39 (1976).
 - [18] N. H. Oliver and P. D. Bons, Mechanisms of fluid flow and fluid–rock interaction in fossil metamorphic hydrothermal systems inferred from vein–wallrock patterns, geometry and microstructure, *Geofluids* **1**, 137 (2001).

- [19] D. Schwabe, P. Hintz, and S. Frank, New features of thermocapillary convection in floating zones revealed by tracer particle accumulation structure (PAS), *Microgr. Sci. Technol.* **9**, 163 (1996).
- [20] J.-J. Xu and S. H. Davis, Convective thermocapillary instabilities in liquid bridges, *Phys. Fluids* **27**, 1102 (1984).
- [21] T. Takakusagi and I. Ueno, Flow patterns induced by thermocapillary effect and resultant structures of suspended particles in a hanging droplet, *Langmuir* **33**, 13197 (2017).
- [22] F. Romanò, H. Wu, and H. C. Kuhlmann, A generic mechanism for finite-size coherent particle structures, *Int. J. Multiphase Flow* **111**, 42 (2019).
- [23] H. Wu, F. Romanó, and H. C. Kuhlmann, Attractors for the motion of a finite-size particle in a two-sided lid-driven cavity, *J. Fluid Mech.* **906**, A4 (2021).
- [24] M. S. Saidov, A. Yusupov, and R. S. Umerov, Si-ge solid solution single crystal growth by electron beam floating zone technique, *J. Cryst. Growth* **52**, 514 (1981).
- [25] A. Eyer, H. Leiste, and R. Nitsche, Floating zone growth of silicon under microgravity in a sounding rocket, *J. Cryst. Growth* **71**, 173 (1985).
- [26] A. Cröll, W. Müller, and R. Nitsche, Floating-zone growth of surface-coated silicon under microgravity, *J. Cryst. Growth* **79**, 65 (1986).
- [27] A. Cröll, T. Kaiser, M. Schweizer, A. N. Danilewsky, S. Lauer, A. Tegetmeier, and K. W. Benz, Floating-zone and floating-solution-zone growth of GaSb under microgravity, *J. Cryst. Growth* **191**, 365 (1998).
- [28] T. A. Campbell, M. Schweizer, P. Dold, A. Cröll, and K. W. Benz, Float zone growth and characterization of $\text{Ge}_{1-x}\text{Si}_x$ ($x \leq 10$ at %) single crystals, *J. Cryst. Growth* **226**, 231 (2001).
- [29] C.-H. Chun and W. Wuest, A micro-gravity simulation of the Marangoni convection, *Acta Astronaut.* **5**, 681 (1978).
- [30] D. Schwabe, A. Scharmann, F. Preisser, and R. Oeder, Experiments on surface tension driven flow in floating zone melting, *J. Cryst. Growth* **43**, 305 (1978).
- [31] F. Preisser, D. Schwabe, and A. Scharmann, Steady and oscillatory thermocapillary convection in liquid columns with free cylindrical surface, *J. Fluid Mech.* **126**, 545 (1983).
- [32] Z. H. Cao, J. C. Xie, Z. M. Tang, and W. R. Hu, The influence of buoyancy on the onset of oscillatory convection in a half floating zone, *Adv. Space Res.* **11**, 163 (1991).
- [33] R. Velten, D. Schwabe, and A. Scharmann, The periodic instability of thermocapillary convection in cylindrical liquid bridges, *Phys. Fluids A* **3**, 267 (1991).
- [34] A. Hirata, S. Nishizawa, and M. Sakurai, Experimental results of oscillatory Marangoni convection in a liquid bridge under normal gravity, *J. Jpn. Soc. Microgr. Appl.* **14**, 122 (1997).
- [35] K. A. Muehler, M. F. Schatz, V. Petrov, W. D. McCormick, J. B. Swift, and H. L. Swinney, Observation of helical traveling-wave convection in a liquid bridge, *Phys. Fluids* **9**, 1850 (1997).
- [36] V. M. Shevtsova, M. Mojahed, and J. C. Legros, The loss of stability in ground based experiments in liquid bridges, *Acta Astronaut.* **44**, 625 (1999).
- [37] Y. Kamotani, L. Wang, S. Hatta, R. Selver, and S. Yoda, Effect of free surface heat transfer on onset of oscillatory thermocapillary flow of high Prandtl number fluid, *J. Jpn. Soc. Microgr. Appl.* **18**, 283 (2001).
- [38] I. Ueno, S. Tanaka, and H. Kawamura, Oscillatory and chaotic thermocapillary convection in a half-zone liquid bridge, *Phys. Fluids* **15**, 408 (2003).
- [39] Y. Kamotani, L. Wang, S. Hatta, A. Wang, and S. Yoda, Free surface heat loss effect on oscillatory thermocapillary flow in liquid bridges of high Prandtl number fluids, *Int. J. Heat Mass Transf.* **46**, 3211 (2003).
- [40] M. Irikura, Y. Arakawa, I. Ueno, and H. Kawamura, Effect of ambient fluid flow upon onset of oscillatory thermocapillary convection in half-zone liquid bridge, *Microgr. Sci. Technol.* **16**, 176 (2005).
- [41] I. Ueno, A. Kawazoe, and H. Enomoto, Effect of ambient-gas forced flow on oscillatory thermocapillary convection of half-zone liquid bridge, *Fluid Dyn. Mater. Process.* **6**, 99 (2010).
- [42] D. Schwabe, F. Preisser, and A. Scharmann, Verification of the oscillatory state of thermocapillary convection in a floating zone under low gravity, *Acta Astronaut.* **9**, 265 (1982).
- [43] R. Monti, On the onset of the oscillatory regimes in Marangoni flows, *Acta Astronaut.* **15**, 557 (1987).
- [44] A. Hirata, M. Sakurai, and N. Ohishi, Effect of gravity on Marangoni convection in a liquid bridge, *J. Jpn. Soc. Microgr. Appl.* **14**, 130 (1997).

- [45] D. Schwabe, Hydrodynamic instabilities under microgravity in a differentially heated long liquid bridge with aspect ratio near the Rayleigh-limit: Experimental results, *Adv. Space Res.* **36**, 36 (2005).
- [46] D. Schwabe, Hydrothermal wave in a liquid bridge with aspect ratio near the Rayleigh limit under microgravity, *Phys. Fluids* **17**, 112104 (2005).
- [47] T. Yano, K. Nishino, H. Kawamura, I. Ueno, S. Matsumoto, M. Ohnishi, and M. Sakurai, Space experiment on the instability of Marangoni convection in large liquid bridge—MEIS-4: Effect of Prandtl number, *J. Phys.: Conf. Ser.* **327**, 012029 (2011).
- [48] H. Kawamura, K. Nishino, S. Matsumoto, and I. Ueno, Report on microgravity experiments of Marangoni convection aboard International Space Station, *J. Heat Transfer* **134**, 031005 (2012).
- [49] T. Yano, K. Nishino, H. Kawamura, I. Ueno, S. Matsumoto, M. Ohnishi, and M. Sakurai, 3-D PTV measurement of Marangoni convection in liquid bridge in space experiment, *Exp. Fluids* **53**, 9 (2012).
- [50] F. Sato, I. Ueno, H. Kawamura, K. Nishino, S. Matsumoto, M. Ohnishi, and M. Sakurai, Hydrothermal wave instability in a high-aspect-ratio liquid bridge of $Pr > 200$, *Microgr. Sci. Technol.* **25**, 43 (2013).
- [51] T. Yano, K. Nishino, H. Kawamura, I. Ueno, and S. Matsumoto, Instability and associated roll structure of Marangoni convection in high Prandtl number liquid bridge with large aspect ratio, *Phys. Fluids* **27**, 024108 (2015).
- [52] K. Nishino, T. Yano, H. Kawamura, S. Matsumoto, I. Ueno, and M. K. Ermakov, Instability of thermocapillary convection in long liquid bridges of high Prandtl number fluids in microgravity, *J. Cryst. Growth* **420**, 57 (2015).
- [53] T. Matsugase, I. Ueno, K. Nishino, M. Ohnishi, M. Sakurai, S. Matsumoto, and H. Kawamura, Transition to chaotic thermocapillary convection in a half zone liquid bridge, *Int. J. Heat Mass Transf.* **89**, 903 (2015).
- [54] T. Yano, K. Nishino, S. Matsumoto, I. Ueno, A. Komiya, Y. Kamotani, and N. Imaishi, Report on microgravity experiments of dynamic surface deformation effects on Marangoni instability in high-Prandtl-number liquid bridges, *Microgr. Sci. Technol.* **30**, 599 (2018).
- [55] S. Tanaka, H. Kawamura, I. Ueno, and D. Schwabe, Flow structure and dynamic particle accumulation in thermocapillary convection in a liquid bridge, *Phys. Fluids* **18**, 067103 (2006).
- [56] M. Wanschura, V. M. Shevtsova, H. C. Kuhlmann, and H. J. Rath, Convective instability mechanisms in thermocapillary liquid bridges, *Phys. Fluids* **7**, 912 (1995).
- [57] D. Schwabe, A. I. Mizev, M. Udhayasankar, and S. Tanaka, Formation of dynamic particle accumulation structures in oscillatory thermocapillary flow in liquid bridges, *Phys. Fluids* **19**, 072102 (2007).
- [58] I. Ueno, Experimental study on coherent structures by particles suspended in half-zone thermocapillary liquid bridges: Review, *Fluids* **6**, 105 (2021).
- [59] T. Sakata, S. Terasaki, H. Saito, S. Fujimoto, I. Ueno, T. Yano, K. Nishino, Y. Kamotani, and S. Matsumoto, Coherent structures of $m = 1$ by low-Stokes-number particles suspended in a half-zone liquid bridge of high aspect ratio: Microgravity and terrestrial experiments, *Phys. Rev. Fluids* **7**, 014005 (2022).
- [60] S. Terasaki, S. Sensui, and I. Ueno, Thermocapillary-driven coherent structures by low-stokes-number particles and their morphology in high-aspect-ratio liquid bridges, *Int. J. Heat Mass Transf.* **203**, 123772 (2023).
- [61] I. Ueno, Y. Abe, K. Noguchi, and H. Kawamura, Dynamic particle accumulation structure (PAS) in half-zone liquid bridge—reconstruction of particle motion by 3-D PTV, *Adv. Space Res.* **41**, 2145 (2008).
- [62] Y. Abe, I. Ueno, and H. Kawamura, Effect of shape of HZ liquid bridge on particle accumulation structure (PAS), *Microgr. Sci. Technol.* **19**, 84 (2007).
- [63] Y. Niigaki and I. Ueno, Formation of particle accumulation structure (PAS) in half-zone liquid bridge under an effect of thermo-fluid flow of ambient gas, *Aerosp. Technol. Jpn.* **10**, 33 (2012).
- [64] D. E. Melnikov, T. Watanabe, T. Matsugase, I. Ueno, and V. Shevtsova, Experimental study on formation of particle accumulation structures by a thermocapillary flow in a deformable liquid column, *Microgr. Sci. Technol.* **26**, 365 (2014).
- [65] H. C. Kuhlmann, R. V. Mukin, T. Sano, and I. Ueno, Structure and dynamics of particle-accumulation in thermocapillary liquid bridges, *Fluid Dyn. Res.* **46**, 041421 (2014).
- [66] A. Toyama, M. Gotoda, T. Kaneko, and I. Ueno, Existence conditions and formation process of second type of spiral loop particle accumulation structure (SL-2 PAS) in half-zone liquid bridge, *Microgr. Sci. Technol.* **29**, 263 (2017).

- [67] M. Gotoda, A. Toyama, M. Ishimura, T. Sano, M. Suzuki, T. Kaneko, and I. Ueno, Experimental study of coherent structures of finite-size particles in thermocapillary liquid bridges, *Phys. Rev. Fluids* **4**, 094301 (2019).
- [68] T. Oba, A. Toyama, T. Hori, and I. Ueno, Experimental study on behaviors of low-stokes number particles in weakly chaotic structures induced by thermocapillary effect within a closed system with a free surface, *Phys. Rev. Fluids* **4**, 104002 (2019).
- [69] K. Yamaguchi, T. Hori, and I. Ueno, Long-term behaviors of a single particle forming a coherent structure in thermocapillary-driven convection in half-zone liquid bridge of high prandtl-number fluid, *Int. J. Microgr. Sci. Appl.* **36**, 360203 (2019).
- [70] M. Takatsuka, S. Tanaka, I. Ueno, and H. Kawamura, Dynamic particle accumulation structure of Marangoni convection in liquid bridge –2. numerical simulation –, in *Proceedings of the Thermal Engineering Conference (in Japanese)* (Japan Society for Mechanical Engineers, 2002), pp. 307–308.
- [71] T. Seki, S. Tanaka, and H. Kawamura, Numerical simulation of particle accumulation structure in oscillatory thermocapillary convection of a liquid bridge, in *Proceedings of the Thermal Engineering Conference (in Japanese)* (Japan Society for Mechanical Engineers, 2005), pp. 169–170.
- [72] D. E. Melnikov, D. O. Pushkin, and V. M. Shevtsova, Accumulation of particles in time-dependent thermocapillary flow in a liquid bridge: Modeling and experiments, *Eur. Phys. J. Spec. Top.* **192**, 29 (2011).
- [73] E. Hofmann and H. C. Kuhlmann, Particle accumulation on periodic orbits by repeated free surface collisions, *Phys. Fluids* **23**, 072106 (2011).
- [74] H. C. Kuhlmann and F. H. Muldoon, Particle-accumulation structures in periodic free-surface flows: Inertia versus surface collisions, *Phys. Rev. E* **85**, 046310 (2012).
- [75] H. C. Kuhlmann and F. H. Muldoon, On the different manifestations of particle accumulation structures (PAS) in thermocapillary flows, *Eur. Phys. J. Spec. Top.* **219**, 59 (2013).
- [76] M. Lappa, On the variety of particle accumulation structures under the effect of g-jitters, *J. Fluid Mech.* **726**, 160 (2013).
- [77] M. Lappa, Assessment of the role of axial vorticity in the formation of particle accumulation structures in supercritical Marangoni and hybrid thermocapillary-rotation-driven flows, *Phys. Fluids* **25**, 012101 (2013).
- [78] D. E. Melnikov, D. O. Pushkin, and V. M. Shevtsova, Synchronization of finite-size particles by a traveling wave in a cylindrical flow, *Phys. Fluids* **25**, 092108 (2013).
- [79] F. H. Muldoon and H. C. Kuhlmann, Coherent particulate structures by boundary interaction of small particles in confined periodic flows, *Physica D* **253**, 40 (2013).
- [80] F. H. Muldoon and H. C. Kuhlmann, Different particle-accumulation structures arising from particle-boundary interactions in a liquid bridge, *Int. J. Multiphase Flow* **59**, 145 (2014).
- [81] F. H. Muldoon and H. C. Kuhlmann, Origin of particle accumulation structures in liquid bridges: Particle-boundary-interactions versus inertia, *Phys. Fluids* **28**, 073305 (2016).
- [82] F. Romanò and H. C. Kuhlmann, Finite-size lagrangian coherent structures in thermocapillary liquid bridges, *Phys. Rev. Fluids* **3**, 094302 (2018).
- [83] R. V. Mukin and H. C. Kuhlmann, Topology of hydrothermal waves in liquid bridges and dissipative structures of transported particles, *Phys. Rev. E* **88**, 053016 (2013).
- [84] T. Ogasawara, K. Motegi, T. Hori, and I. Ueno, Secondary instability induced by thermocapillary effect in half-zone liquid bridge of high Prandtl number fluid, *Mech. Eng. Lett.* **5**, 19 (2019).
- [85] Y. Sasaki, S. Tanaka, and H. Kawamura, Particle accumulation structure in thermocapillary convection of small liquid bridge, in *Proceedings of the 6th Japan/China Workshop on Microgr. Sciences* (2005).

- [86] Y. Fukuda, T. Ogasawara, S. Fujimoto, T. Eguchi, K. Motegi, and I. Ueno, Thermal-flow patterns of $m = 1$ in thermocapillary liquid bridges of high aspect ratio with free-surface heat transfer, *Int. J. Heat Mass Transf.* **173**, 121196 (2021).
- [87] P. Capobianchi and M. Lappa, On the influence of gravity on particle accumulation structures in high aspect-ratio liquid bridges, *J. Fluid Mech.* **908**, A29 (2021).
- [88] P. Capobianchi and M. Lappa, Particle accumulation structures in a 5 cSt silicone oil liquid bridge: New data for the preparation of the JEREMI experiment, *Microgr. Sci. Technol.* **33**, 31 (2021).
- [89] M. Gotoda, T. Sano, T. Kaneko, and I. Ueno, Evaluation of existence region and formation time of particle accumulation structure (PAS) in half-zone liquid bridge, *Eur. Phys. J. Spec. Top.* **224**, 299 (2015).
- [90] I. Barmak, F. Romanò, and H. C. Kuhlmann, Particle accumulation in high-Prandtl-number liquid bridges, *Proc. Appl. Math. Mech.* **19**, e201900058 (2019).
- [91] I. Barmak, F. Romanò, P. K. Kannan, and H. C. Kuhlmann, Coherent particle structures in high-Prandtl-number liquid bridges, *Microgr. Sci. Technol.* **33**, 19 (2021).
- [92] I. Barmak, F. Romanò, and H. C. Kuhlmann, Finite-size coherent particle structures in high-Prandtl-number liquid bridges, *Phys. Rev. Fluids* **6**, 084301 (2021).
- [93] Shin-Etsu Chemical Company Limited, Technical Data: Silicone fluid KF96 Performance Test Results, Tech. Rep. (Shin-Etsu Chemical Co., Ltd., 2014).
- [94] A. D. Pline, Infrared surface temperature measurements for the surface tension driven convection experiment, NASA Technical Memorandum No. 101353 (NASA Lewis Research Center, 1989).
- [95] M. Nishimura, I. Ueno, K. Nishino, and H. Kawamura, 3D PTV measurement of oscillatory thermocapillary convection in half-zone liquid bridge, *Exp. Fluids* **38**, 285 (2005).